(Received 15 January 2025, Accepted 27 February 2025, Scheduled 12 March 2025)

# Optimization of Electromagnetic Thrust for Double-Sided Flux Switching Permanent Magnet Linear Motor

Cheng Wen[1], Aosai Li[1], Mingye Li[2,*], Wei Du[1], Shiming Bai[1], and Xiangyu Meng[1]

[1]*Hebei Provincial Collaborative Innovation Center of Transportation Power Grid Intelligent Integration Technology and Equipment School of Electrical and Electronic Engineering, Shijiazhuang Tiedao University, Hebei 050043, China*
[2]*Hebei University of Engineering Science, Shijiazhuang, Hebei 050091, China*

**ABSTRACT:** Double-Sided Flux Switching Permanent Magnet Linear (DLFSPM) motors are characterized by high efficiency and high power density, which are more and more widely used in various fields, so the design of high-performance linear flux-switching PM motors is of great significance to improving the efficiency of industrial applications. This study aims to achieve the improvement of electromagnetic thrust of double-sided flux switching permanent magnet linear motor by optimizing the motor core structure. First, a theoretical approach is used to construct the motor model and derive the electromagnetic thrust equation. Second, the finite element and Bessel curve fitting methods are used to optimize the core structure to enhance the electromagnetic thrust. Subsequently, the conductive bridge structure is increased to reduce the detent force and improve the performance. Then, the modular structure of primary iron core unit is proposed based on the above two optimizations. Finally, finite element simulation of the proposed optimized structure is carried out to compare the electromagnetic performance of the final comprehensively optimized DLFSPM motor with that of the motor of the initial structure. It is found that the average electromagnetic thrust is increased by 57.85%, and the amplitude of the detent force is reduced by 48.34%, which verifies the effectiveness of the optimization method.

## 1. INTRODUCTION

With the advanced development of industrial technology, the advantages of Double-Sided Flux Switching Permanent Magnet Linear (DLFSPM) motor have become increasingly prominent in related fields such as precision machine tool feed systems, electromagnetic propulsion, and rail transportation [1, 2].

Double-sided flux switching permanent magnet linear motor optimizes the flux path and improves the thrust density and efficiency while reducing the size and weight of the motor through its unique bilateral flux-switching technology [3–5]. This design not only improves the output electromagnetic thrust and dynamic performance of the motor, but also reduces the end effect and improves the overall performance of the motor [6].

The electromagnetic thrust of a linear motor, as a key performance indicator, reflects the size of the motor output capacity [7]; however, due to the unique double convex pole structure and the coalescing effect of the DLFSPM motor, this motor has a higher magnetic flux density, and the magnetic saturation phenomenon usually occurs in some parts of the primary-secondary teeth [8], which results in the existence of the excessive pulsation of the output electromagnetic thrust, mechanical vibration, and noise, greatly affecting the motor operating efficiency and stability [9, 10]. In order to increase the electromagnetic thrust generated by the motor and to reduce the detent force, the structural parameters of the DLFSPM motor must be rationally designed.

* Corresponding author: Mingye Li (15028200250@163.com).

In this paper, the structure of a double-sided flux switching permanent magnet linear motor is optimized, and a two-dimensional finite element model is established for analysis. Firstly, the primary mover core structure of the motor is optimized, including the structure optimization of the permanent magnet end core [11]. Secondly, the conductive bridge structure is added on the basis of the optimized permanent magnet end core [12], and thirdly, the unit modular core structure is proposed on the basis of the above two optimized structures [13]. Finally, the feasibility of the proposed method is verified by finite element simulation analysis.

## 2. DLFSPM MOTOR INITIAL STRUCTURE AND PARAMETERS

### 2.1. Modeling of DLFSPM Motor

The basic structure of double-sided flux switching permanent magnet linear motor is shown in Fig. 1, which consists of two identical long secondary stators and a primary mover. When the motor is running, the middle short mover is driven by the interaction between the armature magnetic field and permanent magnet magnetic field, which has the advantages of simple structure and large electromagnetic thrust.

### 2.2. Electromagnetic Properties of the Initial Model of DLFSPM Motor

Finite element analysis, as a widely accepted method for modeling electric motors, is mainly used for electromagnetic analy-

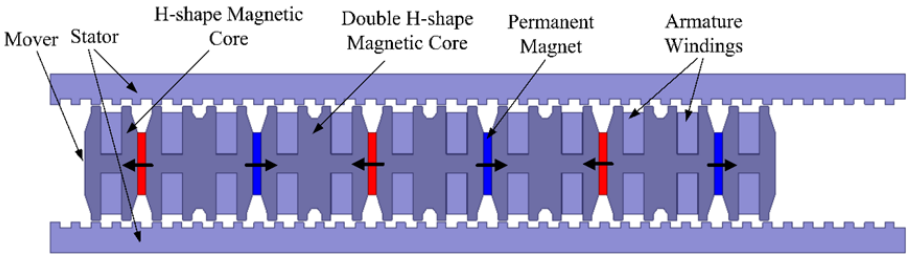


**FIGURE 1**. Initial model of DLFSPM motor.

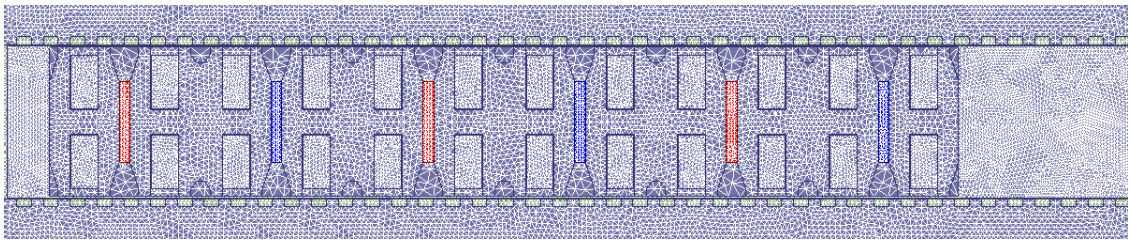

**FIGURE 2**. Mesh sections of DLFSPM motor.

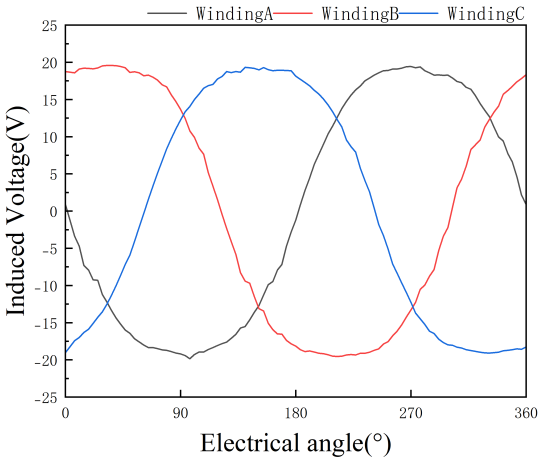


**FIGURE 3**. No-load reverse potential waveforms.

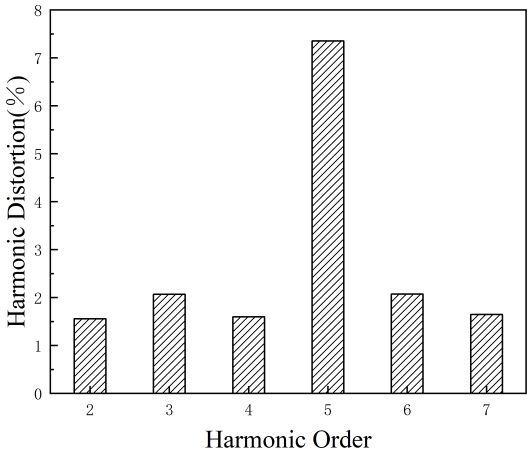


**FIGURE 4**. Harmonic analysis of the opposite electromotive force of A.

sis and structural optimization design of electric motors by decomposing complex geometrical shapes into simple small cells (referred to as finite elements) and performing mathematical analysis on each cell, and then summarizing the results to simulate the behavior of the whole structure. After finite element analysis of the motor, the mesh section structure is shown in Fig. 2.

Figure 3 shows the reverse electromotive force waveforms of the designed DLFSPM motor under no-load condition. As can be seen from the figure, the waveforms of the three reverse electromotive forces are distributed in a sinusoidal structure, and the peak values of the phases are $E_{ma} = 18.51$ V, $E_{mb} = 20.22$ V, and $E_{mc} = 18.45$ V, respectively, which are affected by the end openings, resulting in the magnitude of the reversed electromotive forces of the two phases of A and C being slightly less than the magnitude of the opposite electromotive force of B.

Figure 4 shows the harmonic analysis of the A opposite electromotive force, which yields the ratio of the 3rd harmonic and 5th harmonic amplitudes to the fundamental electromotive force in the A opposite electromotive force to be 2.07% and 7.34%, respectively, and the harmonic effects of the other orders are small and negligible [14]. The total harmonic distortion rate THD (Total Harmonics Distortion) is calculated to be 8.37%.

The distribution of magnetic lines of force has a significant effect on the operation of the flux-switched permanent magnet linear motor and the generation of electromagnetic thrust. As shown in Fig. 5, it is found that there is a serious magnetic leakage problem between the air gaps at the end of the permanent magnets (shown in the black ellipse), and the leakage flux does not traverse the air gaps to participate in the conversion between the electromagnetic energies, which reduces the magnitude of the reaction potential and increases the number of fluctuations in the detent force. The optimization of the motor structure to

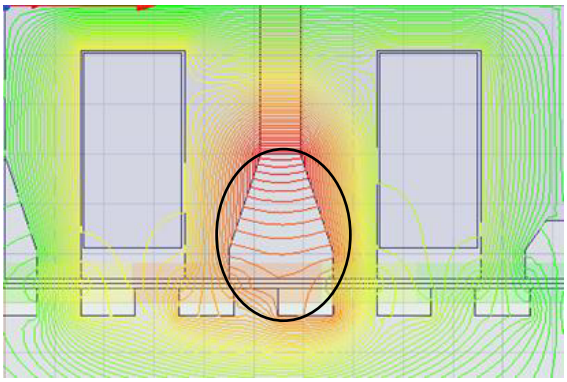

**FIGURE 5**. DLFSPM motor air gap leakage flux.

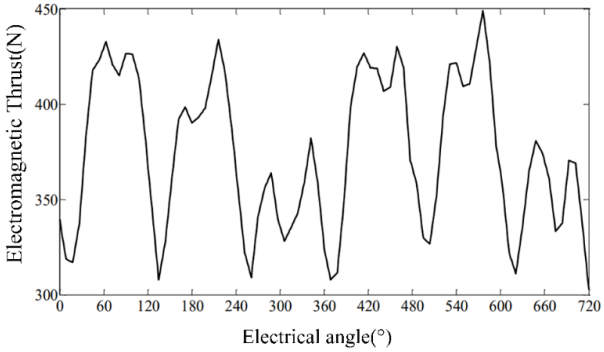


**FIGURE 6**. Electromagnetic thrust of DLFSPM motor.

reduce the magnetic leakage inside the air gap and thus reduce the detent force of the motor and increase the electromagnetic thrust is the focus of this paper.

The output electromagnetic thrust of the DLFSPM motor under the initial structural parameters is shown in Fig. 6, and according to the finite element analysis, the output average electromagnetic thrust of the motor is 374.36 N with a thrust fluctuation of 35.94%.

### 2.3. Electromagnetic Thrust Analysis of DLFSPM Motor

In this study, the electromagnetic thrust of the DLFSPM motor is used as the optimization objective, so it is very important to determine the factors affecting the electromagnetic thrust of the motor before proceeding with the optimization. The electromagnetic thrust of the DLFSPM motor can be determined by combining the work done by the electromagnetic thrust, the displacement of the primary actuator motion, and the magnetic co-energetic method [15, 16]:

$$F_e = \frac{dW}{dx}\Big|_I = F_r + F_{pm} + F_{cog} \tag{1}$$

where $W$ is the work done by the motor electromagnetic thrust, and $x$ is the distance moved by the actuator. $F_r$ is the motor reluctance thrust, $F_{pm}$ the motor permanent magnet thrust, $F_{cog}$ the motor detent force, and these three forces can also be expressed as:

$$F_r = \frac{1}{2} I^T \left(\frac{d}{dx} L\right) I \tag{2}$$

$$\begin{aligned} F_{pm} &= \frac{d}{dx}(\psi_{pm}^T I) = \frac{d\psi_{pma}}{dx} i_a + \frac{d\psi_{pmb}}{dx} i_b + \frac{d\psi_{pmc}}{dx} i_c \\ &= \frac{3}{2}\frac{2\pi}{\tau_s}\psi_m I_m \cos\alpha = \frac{3\sqrt{2}}{2} \\ &\quad \cdot \frac{\pi A_s l_m B_{g\max} l_a c_s k_d k_N \cos_\alpha}{m} \end{aligned} \tag{3}$$

$$F_{cog} = -\frac{d\psi}{dx} i = -R_g \phi \frac{d\phi}{dx} = -\frac{1}{2}\phi_m^2 \frac{dR_g}{dx} \tag{4}$$

Combining the analytical results of Eq. (2), Eq. (3), and Eq. (4), the electromagnetic thrust $F_e$ can be obtained as:

$$F_e = \frac{1}{2} I^T \left(\frac{d}{dx} L\right) I + N_{pm} I \frac{d\phi_m}{dx} - \frac{1}{2}\phi_m^2 \frac{dR_g}{dx} \tag{5}$$

From the analysis of Eq. (5), the main factors affecting the electromagnetic thrust of the DLFSPM motor include the armature current $I$, the dimensions of the motor structure $(l_a, l_m)$, the air-gap magnetic density $(B_g)$, and the number of turns of windings per phase $N_{ph}$. $L$ is the inductance matrix; $I$ is the armature current matrix; $\psi_{pm}$ denotes the permanent magnet flux matrix; $\psi_{pmi}$ represents the permanent magnet flux per phase; $i_a$, $i_b$, and $i_c$ are the three-phase armature currents; $\psi_m$ is the peak permanent magnet flux; $I_m$ is the peak armature current; $\alpha$ denotes the phase difference between armature current and induced electromotive force; $R_g$ is the motor air-gap reluctance; $\phi_m$ is the motor air-gap flux; $\tau_s$ is the motor secondary pole pitch; and $x$ is the motor mover displacement distance.

The inductance $L$ reflects the responsiveness to changes in current, and the electromagnetic thrust increases when the change in the position of the inductance $L$ is large. The air gap flux $\phi_m$ is generated by the permanent magnets, and the electromagnetic thrust increases when its rate of change is large because the change in flux induces an electromotive force in the winding. The number of winding turns $N_{ph}$ affects the inductance of the winding and its response to the magnetic field; the more the winding turns are, the greater the electromagnetic thrust is.

Define the motor thrust fluctuation $F_{rip}$ in percentage form using Eq. (6):

$$F_{rip} = \frac{F_{\max} - F_{\min}}{F_{avg}} \times 100\% \tag{6}$$

Through the electromagnetic characterization of the analytical model of the DLFSPM motor, it is found that the electromagnetic thrust of the motor is closely related to the dimensions of the structural parameters, so it is feasible to optimize the structural parameters of the motor in order to improve the performance of the motor.

## 3. OPTIMIZED DESIGN OF DLFSPM MOTOR CORE STRUCTURE

In actual operation, the detent force and electromagnetic thrust will act on the motor simultaneously. Periodic fluctuations in the detent force are superimposed on the electromagnetic thrust, resulting in fluctuations in the electromagnetic thrust. Therefore, reducing the detent force can effectively reduce the fluctuation of the electromagnetic thrust, improve the stability of the electromagnetic thrust, and also reduce the energy loss and improve the efficiency of the motor. The core structure is optimized for the leakage flux problem between the permanent magnet end and air gap of the DLFSPM motor, and the finite element simulation is used to calculate and change the core structure of the DLFSPM motor to reduce the detent force and increase the electromagnetic thrust.

The basic flow of the motor core structure optimization process is shown in Fig. 7, which describes the process of obtaining a comprehensive optimized structure and comparing its performance by continuously performing structural optimization.

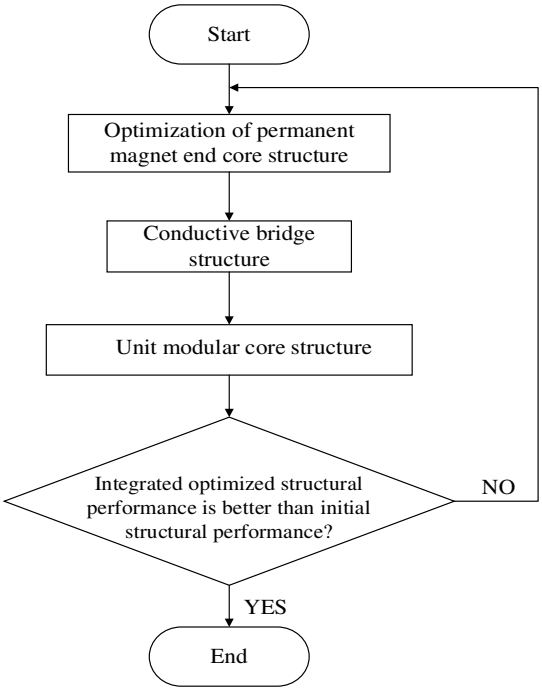


**FIGURE 7**. Optimization process flowchart.

### 3.1. Structural Optimization of Permanent Magnet End Cores for DLFSPM Motor

The presence of flux leakage at the end of the permanent magnet, at the end of the kinematic core, and at the stator teeth results in uneven distribution of flux in the air gap, which in turn leads to increased torque pulsation and reduced counter electromotive force magnitude, which is due to the increase in reluctance due to the sharp edges of the iron core. For this reason, Bessel curve is used to change the edges of the magnetically conductive teeth into circular arcs and optimize the dimensions to increase the effective magnetic flux.

In order to reduce the leakage flux at the end of the permanent magnet, a combination of finite element and second-order Bessel curves is used to fit the arc of the flux lines circulating inside the core to design the most favorable path for the flux circulation. Finally, the curve is used to optimize the structure of the primary core, and the fitting process is shown in Fig. 8.

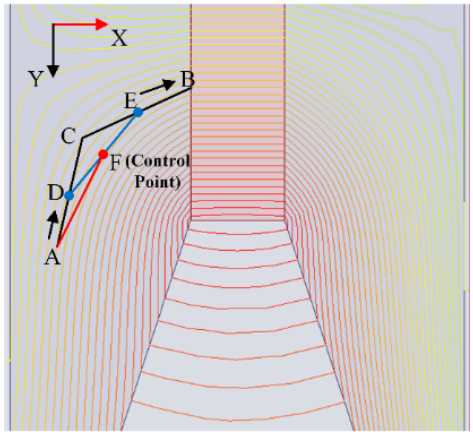


**FIGURE 8**. Bessel curve fitted flux arc curve.

The Bessel curve is utilized to fit the core curvature, which is implemented as follows:

(1) Obtain the magnetic flux line distribution. Using finite element simulation to obtain the motor flux line distribution, three non-collinear points A, B, and C are selected inside the core, where A is located at the flux line without curvature and C located on the surface of the permanent magnet, and the line segments AC and CB are generated.

(2) Determine the proportionality. Choose any point D on the line segment AC and calculate the ratio of AD to AC.

(3) Corresponding Point Mapping. Based on the AD:AC ratio, find the corresponding point E on line segment CB such that $CE : CB = AD : AC$.

(4) Fitting Curve. Connect DE such that $t = AD/AC = CE/CB = DF/DE$, $t \in [0, 1]$, obtain the best-fit curve by adjusting the value of $t$, and generalize it to $N$th-order Bessel curves to find the optimal $t$ value.

(5) Optimization Verification. The fitted curves are used as the optimized shapes of the permanent magnet end cores, and their effectiveness is verified by the finite element method.

where the second-order Bessel curve formula is satisfied:

$$B_2(t) = (1-t)^2 A + 2t(1-t)C + t^2 B, \quad t \in [0,1] \tag{7}$$

$B(t)$ denotes the trajectory of the Bessel curve, and higher order Bessel curves can be expressed as:

$$B_{i,n}(t) = C_n^i t^i (1-t)^{n-i} = \frac{n!}{i!(n-i)!}(1-t)^{n-i}, \quad i \in [0,n] \tag{8}$$

As more orders are obtained, the curve is fitted more accurately. In order to further determine the curve parameters, the

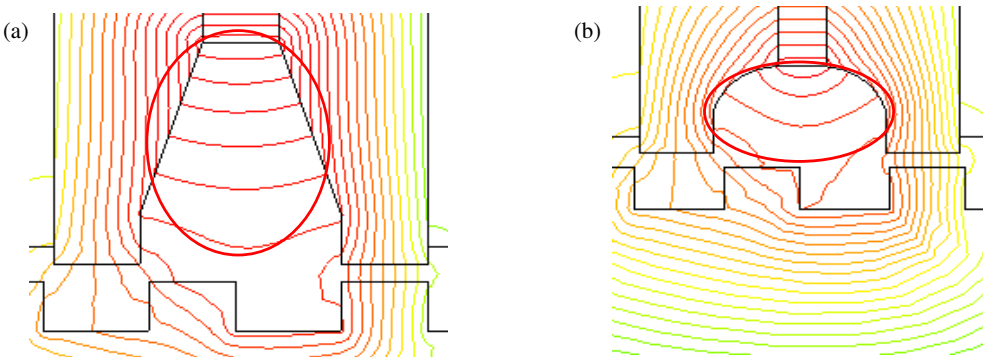


**FIGURE 9**. Comparison of structure and magnetic leakage of permanent magnet end core before and after optimization. (a) Initial model permanent magnet end core structure. (b) Optimized end core structure of permanent magnet.

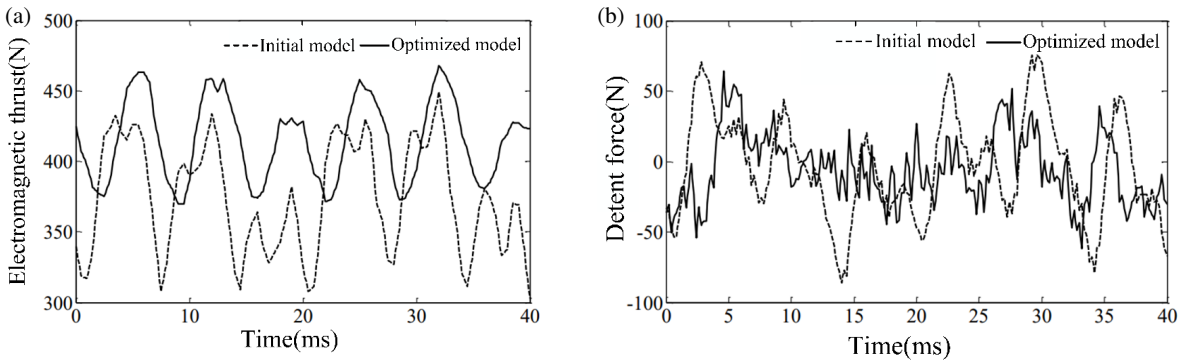


**FIGURE 10**. Comparison of electromagnetic thrust and detent force before and after core optimization. (a) Comparison of electromagnetic thrust waveforms. (b) Comparison of detent force waveforms.

**TABLE 1**. Simulation experiment results for optimizing Bessel curve parameters in DLFSPM motor.

| Order | t value range | Step size | Optimum t-value | Mean electromagnetic force (N) |
|---|---|---|---|---|
| 2 | [0.60, 1.0] | 0.10 | 0.80 | 402.7315 |
| 3 | [0.75, 1.0] | 0.05 | 0.85 | 406.2165 |
| 4 | [0.82, 1.0] | 0.02 | 0.86 | 411.0356 |
| 5 | [0.85, 1.0] | 0.01 | 0.86 | 415.9143 |

following simulation experiment is designed, and the optimal t-value and its range are shown in Table 1.

Table 1 shows the fitting process for the best t-value of Bessel curves with different steps. The step size refers to the incremental size of the parameter $t$ in the Bessel curve fitting process, and a smaller step size can improve the fitting accuracy. The optimal t-value is the parameter value that can make the Bessel curve closest to the target shape. From the data in the table, it can be seen that as the step size of the t-value takes a smaller and smaller value, the t-value of the best fitting curve tends to a constant value, and finally the Bessel curve with a preferred order of 5 and an optimal t-value of 0.86 is preferred to be the shape of the core of the end of the movable permanent magnet. The optimized core structure is shown in Fig. 9.

The flux line distribution obtained from the simulation shows that optimizing the shape of the side edges of the primary magnetizing teeth using Bessel curves effectively reduces the leakage flux at the end of the permanent magnet, and thus the structure makes the rate of change of the flux reluctance between the air gaps decrease. The simulation results are shown in Fig. 10, and the average electromagnetic thrust force after optimization is 400.61 N, which is increased by 6.83% compared with that before optimization. In addition, the amplitude of the detent force is also reduced to a certain extent, thus proving the feasibility of the method.

### 3.2. DLFSPM Motor Added Magnetic Bridge Structure

In order to further reduce the leakage flux at the primary permanent magnet end, a conductive bridge structure is added to the optimization, as shown in Fig. 11.

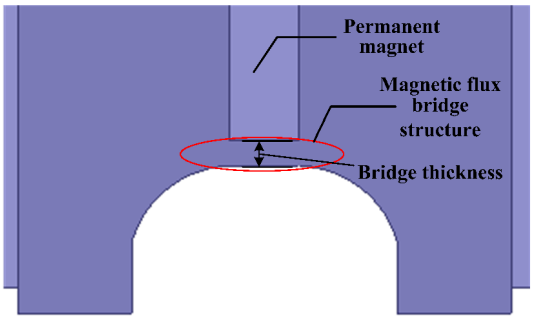


**FIGURE 11**. Conducting flux bridge structure.

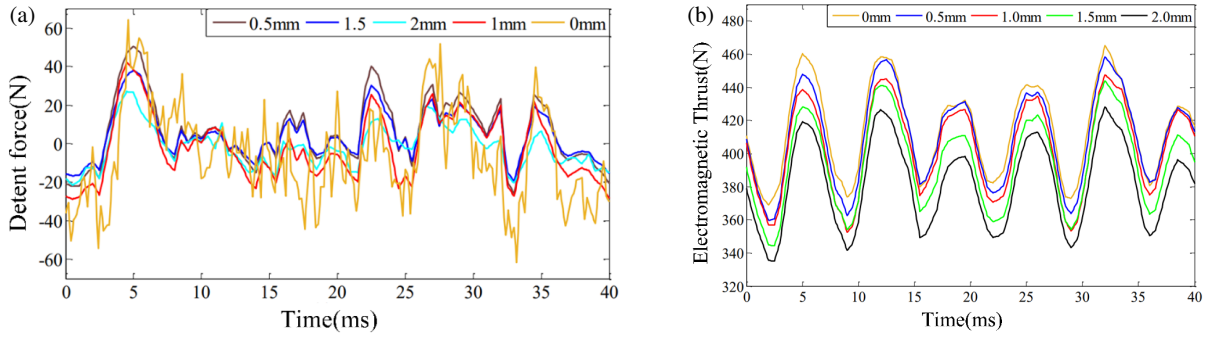


**FIGURE 12**. Comparison of electromagnetic performance of DLFSPM motor with different thickness of magnetic bridge. (a) Detent force for different bridge thicknesses. (b) Electromagnetic thrust for different bridge thicknesses.

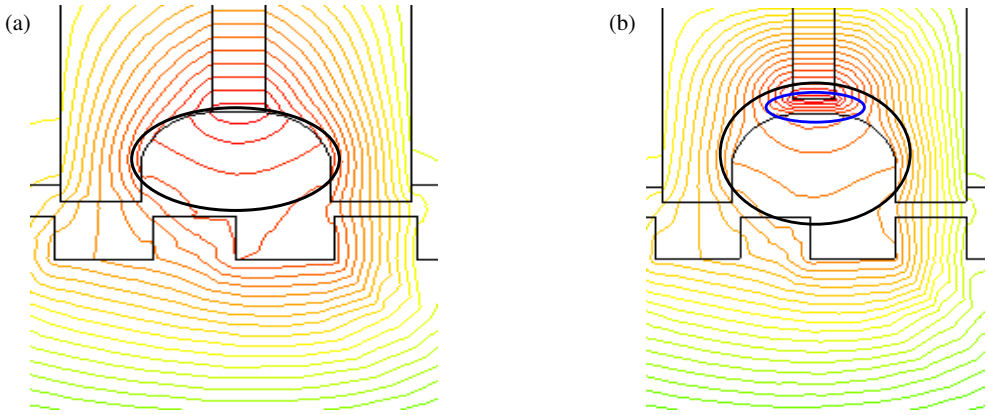


**FIGURE 13**. Leakage flux distribution between air gaps of magnetic bridge structures. (a) Non-magnetic bridge structure. (b) Structure with magnetic bridge.

In order to compare the detent force under different magnetic bridge thicknesses, the thicknesses of the magnetic bridge are set to 0 mm, 0.5 mm, 1.5 mm, and 2 mm. As the thickness of the magnetic bridge increases, the flux path at the end of the permanent magnets forms a loop, and hence the detent force and electromagnetic thrust of the motor decreases. The simulation results of detent force and electromagnetic thrust for different magnetic bridge thicknesses are compared in Fig. 12.

From Figs. 12(a) and (b), it can be found that when the thickness of the magnetic bridge is increased from 0 mm to 2 mm, the detent force decreases significantly, but at the same time, it leads to the loss of electromagnetic thrust, and the larger the thickness of the magnetic bridge is, the more the output electromagnetic thrust decreases. When the thickness of the magnetic bridge is increased to 1 mm, the amplitude of the detent force decreases significantly, decreasing to 34% of the structure without magnetic bridge; when the thickness of the magnetic bridge is increased to 1.5 mm, the detent force decreases only slightly; and when the thickness is increased to 2 mm, the peak of the detent force continues to decrease, but at this time, the electromagnetic thrust force will decrease sharply, while the electromagnetic thrust force continues to decrease in the process of increasing the thickness of the magnetic bridge.

Therefore, a comprehensive consideration is given to minimize the detent force while maintaining the maximized electromagnetic thrust to enhance the dynamic performance of the motor. When the thickness of the magnetic bridge is 1 mm, it is the relatively optimal size to balance the detent force and electromagnetic thrust of the DLFSPM motor.

As shown in the blue elliptical coil in Fig. 13(b), the magnetic bridge structure is an effective way to improve the performance of the DLFSPM motor because the permanent magnet (PM) is inside the primary core and will not be directly exposed to the variations of the reluctance of the convex poles, and it has a better anti-demagnetization performance and lower eddy current loss than the surface-mounted PM in the non-magnetic bridge structure.

As shown in Fig. 14, the magnetic bridge structure causes only a very small amount of partial magnetic saturation in the primary core, which does not cause any significant adverse effect on the operation of the motor, and effectively reduces the detent force of the motor with only a 4.54% loss of electromagnetic thrust compared to the performance of the motor without the magnetic bridge structure.

### 3.3. DLFSPM Motor Adding Unit Modular Core Structure

On the basis of the above optimization, by finite element analysis of the distribution map of the magnetic flux density of the DLFSPM motor in the core of the mover, as shown in the red elliptical coil in Fig. 15, the adjacent permanent magnets (from left to right) are not necessary for the circulation of magnetic

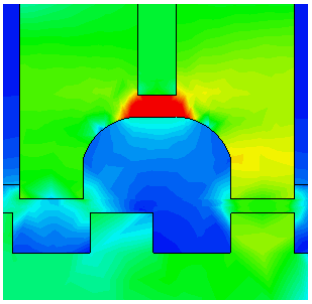

**FIGURE 14**. Magnetic density distribution with magnetic bridge structure.

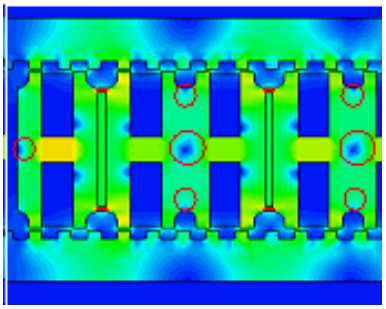

**FIGURE 15**. Magnetic density cloud of DLFSPM motor.

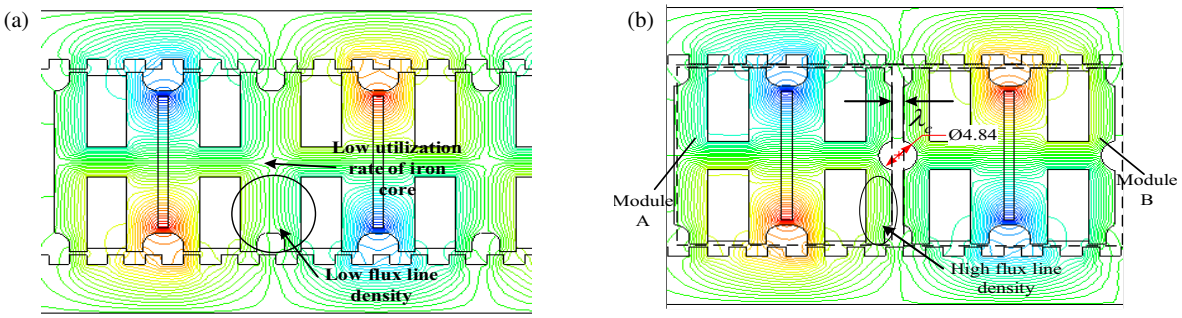


**FIGURE 16**. Flux line distribution of the modular structure of the mover core. (a) Pre-optimization model. (b) Optimized model.

inductance due to the opposite direction of the magnetization, so a part of the core within the primary mover adjacent to each other is unnecessary for the circulation of magnetic inductance and is not conducive to the generation of electromagnetic thrust, so that in order to satisfy mechanical strength, these regions can be minimized.

As shown in Fig. 16, the two magnetic circuits of the adjacent phases are separated to form the structure of the primary kinetochore unitization. As shown by the arrow markings of the primary in Fig. 16(b), the design of the primary core unitization improves the thrust density per unit permanent magnet dosage, and the magnetic inductance circulating between the primary and secondary is denser than the initial structure, Fig. 16(a), which improves the fault-tolerant performance of the DLFSPM motor.

Through the finite element parametric modeling method, the appropriate distance between adjacent units is analytically determined; the adjacent module spacing $\lambda_c$ and circular magnetic barrier radius Ø are set as scanning variables, see Fig. 16(b); the optimal module spacing of 2.85 mm is obtained; and the magnetic flux density within the optimized primary magnetic guide teeth is 1.07 T, which has not reached magnetic saturation at a relatively high degree. The optimum magnetic barrier radius is also obtained as 4.84 mm, and the optimized primary core usage is reduced by 22.39% compared to the initial motor.

On the basis of the optimized structure in the previous section, the waveform of electromagnetic thrust with the addition of kinetic unitization is shown in Fig. 17, and the average electromagnetic thrust is increased by 19.38%, which verifies that the unit modular core structure is a more effective method to increase the output electromagnetic thrust of the motor.

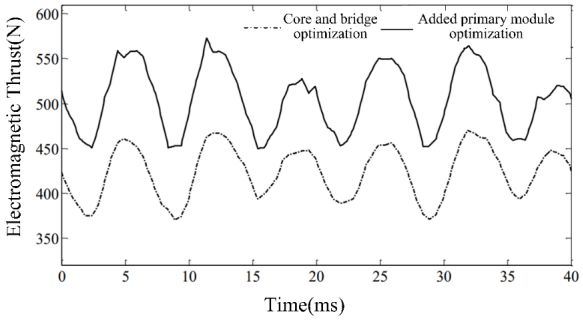


**FIGURE 17**. Comparison of thrust waveforms for modular structure of actuator core.

### 3.4. Comparison of Electromagnetic Performance before and after Optimized Structure

Through the above optimization method and finite element simulation, the performance of the comprehensively optimized DLFSPM motor is compared with that of the initial motor, and the reduction of the detent force and the increase of the average electromagnetic thrust are selected as the main comparison objectives. The initial motor structure and the comprehensively optimized structure of the primary core are represented by A1 and A2, as shown in Figs. 18 and 19, respectively.

From the comparative analysis of waveforms of detent force in Fig. 20, it can be concluded that the method of optimizing the iron core for the purpose of reducing the leakage flux of the motor can effectively reduce the magnitude of the detent force, and the magnitude of the detent force of the comprehensive optimized structure has been reduced by 48.34% compared with the initial structure.

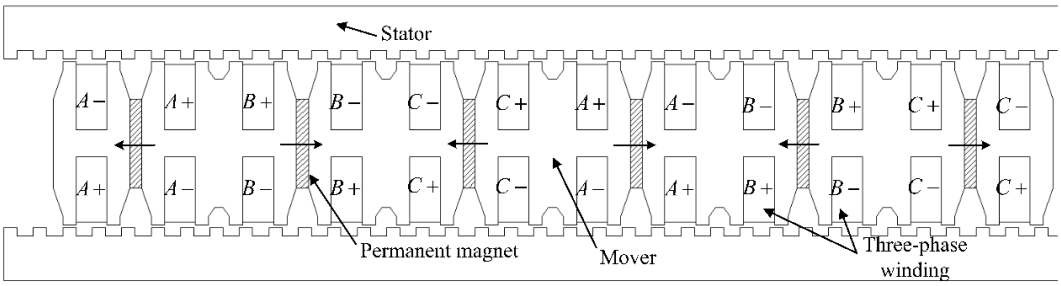


**FIGURE 18**. Initial structure of DLFSPM motor (A1).

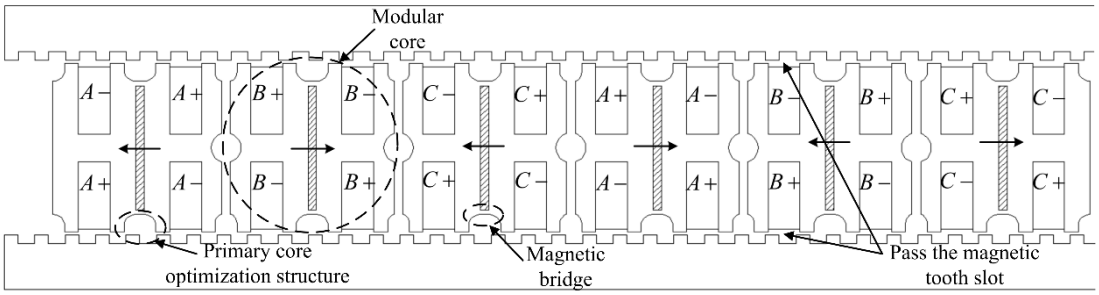


**FIGURE 19**. DLFSPM motor primary core integrated optimized structure (A2).

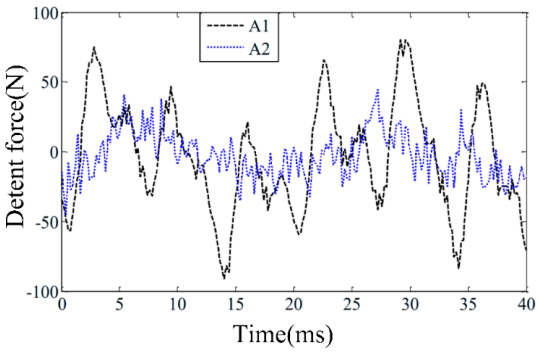


**FIGURE 20**. Detent force waveform comparison before and after optimization.

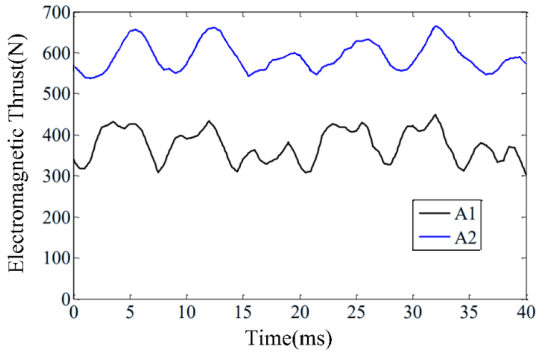


**FIGURE 21**. Electromagnetic thrust waveform comparison before and after optimization.

Figure 21 shows the comparison of the thrust performances of the DLFSPM motor before and after the optimization, and it can be seen from the simulation result plots that the electromagnetic thrust of the motor is significantly increased after the comprehensive optimization of the primary core of the motor under the same secondary pole spacing, the same air gap, and the same current excitation conditions.

A comprehensive comparison of electromagnetic thrust performances before and after optimization is given in Table 2, which includes a comparative analysis of thrust density, i.e., the electromagnetic thrust generated per unit volume of permanent magnets in linear motors under rated conditions, and also reflects the material utilization.

As can be seen from Fig. 22(a), the comprehensive optimization method adopted in this paper increases the magnitude of the counterpotential, which is 19.46 V for the initial (A1), and the magnitude of the counterpotential is 22.58 V for the optimized (A2), which is an increase of 16.07%; the harmonic analysis of the counterpotentials before and after the optimization is carried out in Fig. 22(b), which shows that the counterpotential of the initial structure (A1) contains a high number of harmonic components, and the harmonic distortion rate is 7.84%, of which the 3rd, 5th, and other odd harmonics are the main components. After the comprehensive optimization of the primary core structure of the motor (A2), the THD is reduced to 5.63%, which has a significant suppression effect.

In optimizing the core structure at the end of the mover's permanent magnet, the amount of permanent magnets and the armature excitation are kept constant. The addition of a conductive bridge structure changes the permanent magnet to an insertion type and reduces the complexity of fabrication. The proposed method of modular structure optimization of the kinematic core unit minimizes the structure that is unfavorable to the magnetic inductance flow, while separating the adjacent phase

**TABLE 2**. Thrust performance comparison before and after optimization.

| Project | Mean electromagnetic thrust (N) | Thrust ripple $T_r$ (%) | Thrust density (N/mm$^3$) | Detent force ratio (%) |
|---|---|---|---|---|
| Initial structure (A1) | 374.363 | 39.145 | 0.207 | 21.436 |
| Core comprehensive optimization (A2) | 590.915 | 21.680 | 0.328 | 7.492 |

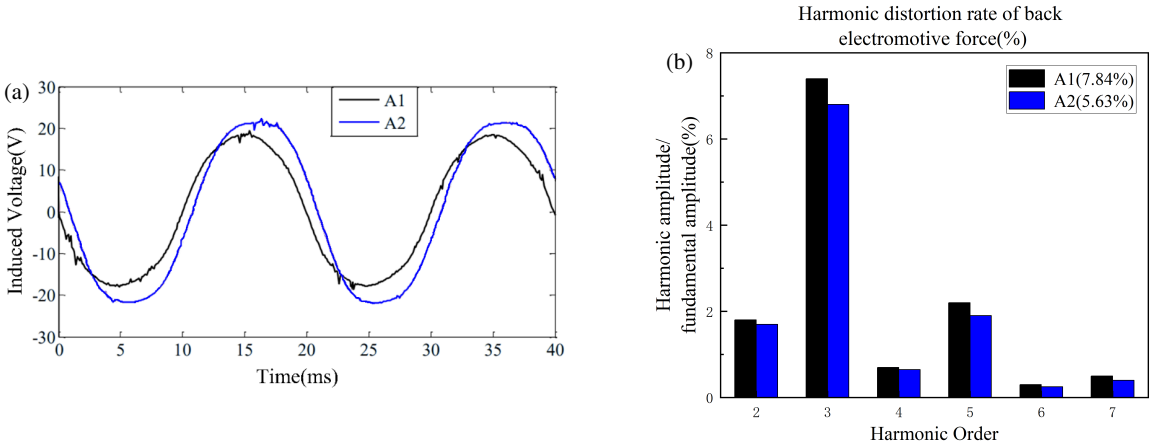


**FIGURE 22**. Comparison of reverse electromotive force before and after optimization. (a) Comparison of reverse electromotive force waveforms before and after optimization. (b) FFT analysis of the inverse electromotive force before and after optimization.

magnetic circuits to form the primary kinematic unit structure, which is conducive to the heat dissipation of the motor, and the optimized primary core dosage is reduced by 22.39%, which reduces the material cost.

## 4. CONCLUSION

In this paper, the purpose of increasing the motor output electromagnetic thrust and reducing the thrust fluctuation is achieved by comprehensively optimizing the structure of the movable iron core of the DLFSPM motor. The method utilizes Bessel curves to optimize the shape of the side edges of the primary magnet-conducting teeth, increases the magnet-conducting bridge structure based on the optimization of the permanent magnet end cores, and carries out the unit modular design of the primary iron core on the basis of the above two optimization methods, which is experimentally verified by finite element analysis. This comprehensive optimization method aims to increase the average electromagnetic thrust, reduce the detent force amplitude, decrease the thrust fluctuation, and increase the thrust density. The results show that compared with the initial structure, the average electromagnetic thrust increases by 57.85%; the ratio of detent force amplitude to average electromagnetic thrust decreases by 13.94%; the thrust fluctuation decreases by 17.47%; and the thrust density increases by 0.121 N/mm$^3$. This comprehensive optimization method realizes the optimization of the output electromagnetic thrust of the motor and improves the stability of the operation of the motor and the output performance.

## ACKNOWLEDGEMENT

This work was supported in part by National Natural Science Foundation of China under Grant 51807124, Natural Science Foundation of China's Hebei Province under Grant E2021210069 and A2022210024, funded by Science and Technology Project of Hebei Education Department under Grant QN2020155. Hebei Graduate Student Innovation and Entrepreneurship Funding Project under Grant YC202545.

## REFERENCES

[1] Sun, Z., L. Xu, W. Zhao, and K. Du, "Comparison between linear induction motor and linear primary permanent magnet vernier motor for railway transportation," in *2021 13th International Symposium on Linear Drives for Industry Applications (LDIA)*, 1–6, Wuhan, China, Jul. 2021.

[2] Liu, X., C. Hu, X. Li, J. Gao, and S. Huang, "An online data-driven multi-objective optimization of a permanent magnet linear synchronous motor," *IEEE Transactions on Magnetics*, Vol. 57, No. 7, 1–4, Jul. 2021.

[3] Zhao, W., A. Ma, J. Ji, X. Chen, and T. Yao, "Multiobjective optimization of a double-side linear Vernier PM motor using response surface method and differential evolution," *IEEE Transactions on Industrial Electronics*, Vol. 67, No. 1, 80–90, Jan. 2020.

[4] Zhang, Y., J. Xu, Z. Han, Z. Wu, C. Huang, and M. Li, "System-level optimization design of tubular permanent-magnet linear synchronous motor for electromagnetic emission," in *2021 13th International Symposium on Linear Drives for Industry Applications (LDIA)*, 1–4, Wuhan, China, 2021.

[5] Wang, W., J. Zhao, Y. Zhou, and F. Dong, "New optimization design method for a double secondary linear motor based on R-DNN modeling method and MCS optimization algorithm," *Chinese Journal of Electrical Engineering*, Vol. 6, No. 3, 98–105, 2020.

[6] Accetta, A., F. Alonge, M. Cirrincione, F. D'Ippolito, M. Pucci, and A. Sferlazza, "GA-based off-line parameter estimation of the induction motor model including magnetic saturation and iron losses," *IEEE Open Journal of Industry Applications*, Vol. 1, 135–147, 2020.

[7] Dong, F., J. Zhao, J. Song, Y. Feng, and Z. He, "Optimal design of permanent magnet linear synchronous motors at multispeed based on particle swarm optimization combined with SN ratio method," *IEEE Transactions on Energy Conversion*, Vol. 33, No. 4, 1943–1954, 2018.

[8] Wen, C., Q. Zhao, M. Li, J. Liu, M. Li, and X. Zhao, "Multi-objective optimization based on hyperparameter random forest regression for linear motor design," *International Journal of Machine Learning and Cybernetics*, Vol. 13, No. 10, 2929–2942, 2022.

[9] Hu, C., H. Cui, X. Li, X. Liu, and S. Huang, "Thrust characteristic improvement of permanent magnet linear synchronous motor based on multiobjective optimization," in *2021 13th International Symposium on Linear Drives for Industry Applications (LDIA)*, 1–5, Wuhan, China, Jul. 2021.

[10] Liu, Y., X. Huang, J. Li, and W. Yu, "Magnetic field analysis and thrust optimization of ARC permanent magnet synchronous motor combined with linear mover and ARC stator," *IEEE Transactions on Industry Applications*, Vol. 59, No. 5, 5867–5874, Sep.-Oct. 2023.

[11] Wu, S. and Q. Lu, "Eddy current analysis and optimization design of the secondary of the linear induction motor with an approximation and prediction method," *IEEE Transactions on Magnetics*, Vol. 58, No. 2, 1–5, Feb. 2022.

[12] Li, C., Z. Lan, B. Cai, and Q. Zheng, "Vector control strategy of permanent magnet synchronous linear motor based on sliding mode speed controller and model reference adaptive," in *2021 13th International Symposium on Linear Drives for Industry Applications (LDIA)*, 1–5, Wuhan, China, Jul. 2021.

[13] Hu, H., X. Liu, J. Zhao, and Y. Guo, "Analysis and minimization of detent end force in linear permanent magnet synchronous machines," *IEEE Transactions on Industrial Electronics*, Vol. 65, No. 3, 2475–2486, 2018.

[14] Nie, L. and J. Fang, "Optimization of coreless high temperature superconducting linear synchronous motor," *IEEE Transactions on Applied Superconductivity*, Vol. 34, No. 8, 3603704, Nov. 2024.

[15] Wu, L., Y. Li, Q. Lu, and Y. Fang, "Detent-force analysis and reduction of modular permanent-magnet linear synchronous motors with non-overlapping windings," in *2023 14th International Symposium on Linear Drivers for Industry Applications (LDIA)*, 1–5, Hannover, Germany, 2023.

[16] Ji, J., X. Zhu, H. Tang, L. Xu, and W. Zhao, "Design to improve thrust force performance of dual-side primary permanent-magnet vernier linear motor," *Chinese Journal of Electrical Engineering*, Vol. 9, No. 2, 1–13, Jun. 2023.